Available online at www.sciencedirect.com

SCIENCE DIRECT®

Comput. Methods Appl. Mech. Engrg. 192 (2003) 3317–3341

Computer methods in applied mechanics and engineering

www.elsevier.com/locate/cma

An adaptive finite element method for Bingham fluid flows around a cylinder

Nicolas Roquet, Pierre Saramito *

LMC-IMAG, B.P. 53, 38041 Grenoble cedex 9, France

Received 8 March 2002; received in revised form 6 March 2003; accepted 19 March 2003

Abstract

The numerical modeling of the steady flow of a yield stress fluid around a cylinder is presented. Three categories of yielded regions are exhibited. The asymptotic behavior when the cylinder gets close to the wall is investigated. The resolution of variational inequalities describing the flow is based on the augmented Lagrangian method and a mixed finite element method. The localization of yield surfaces is approximated by an anisotropic auto-adaptive mesh procedure.

Keywords: Yield stress fluids; Bingham model; Variational inequalities; Flow around a cylinder; Adaptive mesh; Mixed finite element methods

1. Introduction

1.1. Overview

In this article, we study the wall effect on the flow of a Bingham fluid around a cylinder falling at constant speed between two parallel plates (see Fig. 1). This problem may be seen as the starting point for the study of more complex flows with particles. It can also be considered as a benchmark for testing the accuracy of the numerical method which is used to solve it, because it contains many difficulties of different kind. Indeed, in such a flow, some rigid zones are very small and hence are a priori difficult to get accurately.

Our problem and an analogous one, the flow around a spherical particle, have been intensively studied for viscoelastic materials (see e.g. the recent numerical work of Huang and Feng [1] and the references therein on the wall effect for the cylinder). Concerning yield stress fluid, references on the cylinder case are seldom. The first experimental works lie in Yoshioka and Adachi [2] and in Brooks and Whitmore [3,4] where the drag coefficient is studied. To our knowledge, there exist no numerical works on the problem presented here.

---

* Corresponding author. Tel.: +33-4-76-51-46-10; fax: +33-4-76-63-12-63.
E-mail address: pierre.saramito@imag.fr (P. Saramito).

0045-7825/03/$ - see front matter © 2003 Elsevier B.V. All rights reserved.
doi:10.1016/S0045-7825(03)00262-7

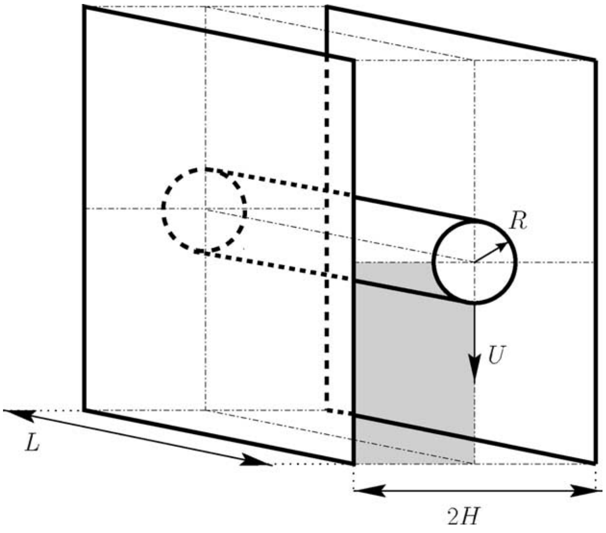

Fig. 1. Cylinder with radius R moving at constant speed U between two parallel plates.

However, recent numerical works deal with the close case of the spherical particle. Beris et al. [5] have studied the case of an infinite medium by a domain transformation method with the biviscous model of Bercovier–Engelman [6]. Blackery and Mitsoulis [7] were interested in the wall effect. They used a finite element method and the biviscous method of Papanastasiou and Tasos [8]. They considered a ratio tube/particle $\geqslant 2$. This case will be called here "far from cylinder". The same study is carried out by Beaulne and Mitsoulis [9] with the Papanastasiou's regularization of the Herschel–Bulkley model.

Several experimental works dealt with the spherical particle case, in the situation "far from cylinder". A detailed survey was carried out by Chhabra and Uhlherr [10]. The recent work of Atapattu et al. [11,12] must be added to this survey, concerning especially the wall effect and the shape of the boundary of the shared zones.

Finally, as far as we know, it appears in literature that

- the case of the cylinder has never been numerically investigated for viscoplastic models;
- in both experimental and numerical works dealing with the close case of a spherical particle, the situation where the wall is very close to the particle is never considered (i.e. when the ratio tube/particle is lower than 2).

These are the reasons why, in the present work, an original study is given, in which the wall effect is numerically computed, in the case of the cylinder, in the situation "near the cylinder", i.e. when the gap between the wall and the cylinder becomes small compared to the radius of the cylinder. The behavior of the velocity and the stress will be established. In particular, the boundary of the shared zones and the drag coefficient will be accurately determined.

1.2. General aspect

Let us begin with the global aspect of the flow Fig. 2. We also introduce a specific and concise terminology. The flow can be viewed as four kinds of distinct zones:

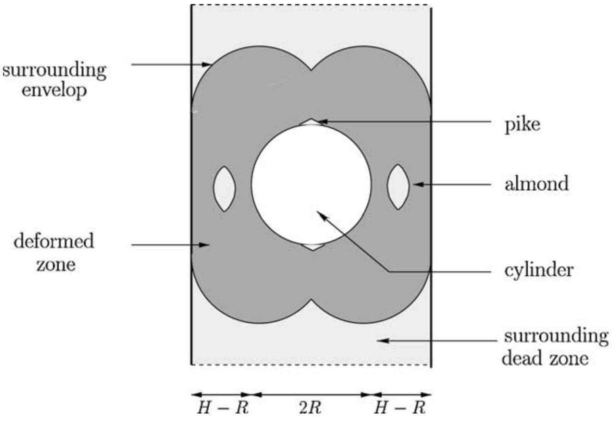

Fig. 2. Schematic cut view: deformed zones in dark grey, rigid zones in light grey, cylinder cross section in white.

(1) A *surrounding dead zone* contains the deformed zone. This plastic zone and the deformed zone are the viscoplastic material within the cylinder is moving.
(2) A *deformed zone* lies around the cylinder. Its boundary with the surrounding dead zone is called the *surrounding envelop*. This envelop touches the wall. Beris et al. [5] have determined a similar shape in the case of spherical particle in an infinite media.
(3) Two rigid pike-shaped zones are located on the axis of the flow. These two *pikes* stick in front of and behind the cylinder, and are always included within the deformed zone. In the analogous problem of the spherical particle, they are sometimes called "polar caps" in the literature.
(4) Two oval rigid zones with pointed extremities, called *almonds*, lie inside the deformed zone. Both are located within the deformed zone, between the wall and the cylinder, symmetrically with respect to the axis of the flow.

Both the shape of the deformed zone and the existence of the pike are familiar to readers interested in yield stress fluid flows around a translating object. Indeed, authors dealing with the flow of viscoplastic material around a spherical particle establish those phenomena (at least for $\alpha \geqslant 1$). This leads to a discussion on the precise shape of the envelop and of the pike, with respect to parameters such as α and Bi (see for instance several references concerning the pike and the envelop in the survey by Chhabra and Uhlherr [10]). On the other hand, the existence of almonds is an original aspect, which has never been mentioned for the Bingham model. It has to be noted that the few works dealing with the cylinder have never bought to light the shape of the rigid zones and hence of the almond in particular. In the case of the spherical particle, Beaulne and Mitsoulis [9] have obtained a phenomenon analogous to almonds, in a numerical simulation, using the biviscous model of Papanastasiou Tasos [8] for the Herschel–Bulkley model. In this case, it is more suitable to speak of an "annulus" of rigid material surrounding the spherical particle. Beaulne and Mitsoulis use the word "island", instead of annulus. In this particular case, the existence of such an annulus is possible only if the velocity field in this zone consists only in a translation parallel to the axis of the flow. Indeed, if the rotation component of the velocity is non-zero, then the rigid annulus must be deformed: we are led to a contradiction, and the annulus cannot exist in the axisymmetric case. In addition, Beris et al. [5] notice the presence of a torus-shaped region where the velocity field is "close" to the one of a rigid solid. They also point out that it is impossible to have a rigid zone in this torus.

2. Problem statement

The Bingham model [13,14] is characterized by the following property: the material starts to flow only if the applied forces exceed a certain limit σ_0, called the yield limit. The total Cauchy stress tensor is expressed by

$$\sigma_{\mathrm{tot}} = -p \cdot I + \sigma,$$

where σ denotes its deviatoric part, and p is the pressure. The conservation of momentum is

$$\rho\left(\frac{\partial \mathbf{u}}{\partial t} + \mathbf{u}\cdot\nabla\mathbf{u}\right) - \mathbf{div}\,\sigma + \nabla p = 0,$$

where $\mathbf{u}$ is the velocity field, and ρ the constant density. Since the fluid is assumed to be incompressible, the mass conservation leads to

$$\operatorname{div}\mathbf{u} = 0. \tag{1}$$

The constitutive equation can be written as

$$\begin{aligned} &\sigma = 2\eta D(\mathbf{u}) + \sigma_0 \frac{D(\mathbf{u})}{\|D(\mathbf{u})\|} && \text{if } \|D(\mathbf{u})\| \neq 0, \\ &\|\sigma\| \leqslant \sigma_0 && \text{if } \|D(\mathbf{u})\| = 0 \end{aligned} \tag{2}$$

or equivalently:

$$D(\mathbf{u}) = \begin{cases} \left(1 - \dfrac{\sigma_0}{\|\sigma\|}\right)\dfrac{\sigma}{2\eta} & \text{if } \|\sigma\| > \sigma_0, \\ 0 & \text{otherwise,} \end{cases}$$

where $\sigma_0 \geqslant 0$ is the yield stress, $\eta > 0$ is the plastic viscosity, $D(\mathbf{u}) = (\nabla\mathbf{u} + \nabla\mathbf{u}^{\mathrm{T}})/2$ is the rate-of-deformation tensor, and, for any tensor $\tau = (\tau_{ij})$, the notation $\|\tau\|$ represents the following matrix norm:

$$\|\tau\| = \sqrt{\tau : \tau} = \left(\sum_{ij} \tau_{ij}^2\right)^{1/2}.$$

Notice that for $\sigma_0 = 0$, one obtains the classical viscous incompressible fluid. When $\sigma_0 > 0$, rigid zones in the interior of the fluid can be observed. As σ_0 becomes larger, these rigid zones develop.

We consider an infinite cylinder moving between two parallel plates at constant speed U (see Fig. 1). The medium between the two plates and the cylinder is a viscoplastic fluid, described by the Bingham model. Let R be the radius of the cylinder and $2H$ be the distance between the two plates. A characteristic viscous stress is given by $\Sigma = \eta U/R$. The dimensionless Bingham number is defined as the ratio of the yield stress to a representative viscous stress:

$$Bi = \frac{\sigma_0 R}{U\eta}.$$

A dimensionless number characterizing the geometry is the ratio of the gap between the plate and the cylinder to the radius of the cylinder:

$$\alpha = \frac{H - R}{R}.$$

The flow is supposed to be slow and the inertial effects are neglected. We are looking for the stationary flow. Thus, the conservation of momentum reduces to

$$\mathbf{div}\,\sigma - \nabla p = 0. \tag{3}$$

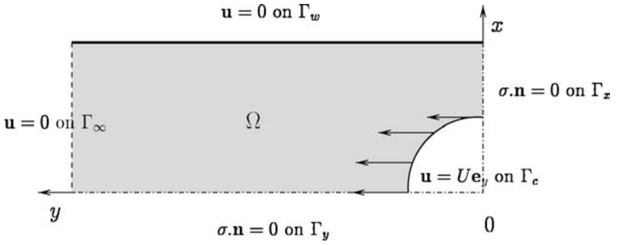

Fig. 3. The domain of computation and the boundary conditions.

Let Oz be the axis of the cylinder, Ox be orthogonal to the plates and Oy such that (O, x, y, z) is direct. Remarking that the flow is independent of z and symmetric with respect to Ox and Oy, the domain of computation Ω is reduced consequently (see Fig. 3).

Let Γ_x (resp. Γ_y) be the intersection of $\partial\Omega$ with the axis Ox (resp. Oy). The homogeneous Neumann boundary condition on symmetry axis writes

$$\sigma \cdot \mathbf{n} = \mathbf{0} \quad \text{on } \Gamma_x \cup \Gamma_y. \tag{4}$$

The Dirichlet boundary condition along the intersection Γ_c of the cylinder with $\partial\Omega$ writes

$$\mathbf{u} = U\mathbf{e}_x \quad \text{on } \Gamma_\mathrm{c}. \tag{5}$$

The domain Ω is bounded in the Ox_1 direction, and its length, denoted L is supposed to be sufficiently large for the flow to be fully developed i.e. when the velocity vanishes. Let Γ_∞ denote the corresponding part of $\partial\Omega$. The velocity vanishes also along the plates Γ_w. This leads to the following homogeneous Dirichlet boundary condition:

$$\mathbf{u} = 0 \quad \text{on } \Gamma_\infty \cup \Gamma_w. \tag{6}$$

The problem writes

(P): find $\mathbf{u}$ and σ satisfying (1)–(6).

3. Numerical method

3.1. Augmented Lagrangian algorithm

Let X_U and V_U denote the following convex sets:

$$X_U = \{\mathbf{v} \in (H^1(\Omega))^2; \mathbf{v} = 0 \text{ on } \Gamma_0 \text{ and } \mathbf{v} = -U\mathbf{e}_2 \text{ on } \Gamma_D\},$$

$$V_U = \{\mathbf{v} \in X_U; \operatorname{div}\mathbf{v} = 0 \text{ in } \Omega\},$$

and J the following functional:

$$J(\mathbf{v}) = \sigma_0 \int_\Omega \|D(\mathbf{v})\|\,\mathrm{d}x + \eta \int_\Omega \|D(\mathbf{v})\|^2\,\mathrm{d}x.$$

Glowinski et al. [15] showed that the solution $\mathbf{u}$ of problem (P) expressed as a minimization point of J on V_U:

$$\min_{\mathbf{v}\in V_U} J(\mathbf{v}). \tag{7}$$

Since J is non-differentiable on V_U when $\sigma_0 > 0$ due to the term $\int_\Omega \|D(\mathbf{v})\|\,\mathrm{d}x$, the problem cannot be described by an equation and thus requires a specific convex optimization approach (see e.g. [16]).

Let us introduce $T = \{\tau \in (L^2(\Omega))^4; \tau^{\mathrm{T}} = \tau\}$ the space of square integrable symmetric second order tensors. Then

$$\gamma = D(\mathbf{u}) \in T. \tag{8}$$

The linear constraint (8) is handled by using a Lagrange multiplier that coincides with the stress $\sigma \in T$:

$$\mathscr{L}(\mathbf{u}, \gamma; \sigma) = \sigma_0 \int_\Omega \|\gamma\|\,\mathrm{d}x + \eta \int_\Omega \|\gamma\|^2\,\mathrm{d}x + \int_\Omega (D(\mathbf{v}) - \gamma) : \sigma\,\mathrm{d}x.$$

For all $r > 0$, the augmented Lagrangian

$$\mathscr{L}_r(\mathbf{u}, \gamma; \sigma) = \mathscr{L}(\mathbf{u}, \gamma; \sigma) + r \int_\Omega \|D(\mathbf{v}) - \gamma\|^2\,\mathrm{d}x$$

is quadratic and positive definite with respect to $\mathbf{u}$. This implies that with σ and γ fixed, $\mathscr{L}_r$ can be minimized with respect to $\mathbf{u}$ on V_U, whereas this operation is impossible in practice for $r = 0$. This transformation is helpful since we can find the saddle-point of $\mathscr{L}_r$, which coincides with those of $\mathscr{L}$, by an appropriate algorithm proposed in [17,18].

Algorithm 3.1 (*Uzawa for Bingham*).

initialization $n = 0$

Let γ^0 and σ^0 arbitrarily chosen in T.

loop $n \geqslant 1$

- **step 1**: Assume γ^n and σ^n are known, find $\mathbf{u}^{n+1}$ and p^{n+1} satisfying

$$-r\Delta\mathbf{u}^{n+1} + \nabla p^{n+1} = \mathbf{div}(\sigma^n - 2r\gamma^n) \quad \text{in } \Omega, \tag{9}$$

$$\operatorname{div}\mathbf{u}^{n+1} = 0 \quad \text{in } \Omega, \tag{10}$$

$$2rD(\mathbf{u}^{n+1}) \cdot \mathbf{n} = (2r\gamma^n - \sigma^n) \cdot \mathbf{n} \quad \text{on } \Gamma_N, \tag{11}$$

$$\mathbf{u}^{n+1} = -U\mathbf{e}_2 \quad \text{on } \Gamma_D, \tag{12}$$

$$\mathbf{u}^{n+1} = 0 \quad \text{on } \Gamma_0. \tag{13}$$

- **step 2**: compute explicitly γ^{n+1} as

$$\gamma^{n+1} := f(\sigma^n + 2rD(\mathbf{u}^{n+1})) \quad \text{in } \Omega. \tag{14}$$

- **step 3**: compute explicitly σ^{n+1} as

$$\sigma^{n+1} := \sigma^n + 2r(D(\mathbf{u}^{n+1}) - \gamma^{n+1}) \quad \text{in}\,\Omega \tag{15}$$

with the notation

$$f(\tau) = \begin{cases} 0 & \text{if } \|\tau\| < \sigma_0, \\ \left(1 - \dfrac{\sigma_0}{\|\tau\|}\right) \dfrac{\tau}{2(r+\eta)} & \text{otherwise} \end{cases}$$

for any second order matrix τ. The interest of this algorithm is that it transforms the global non-differentiable problem into a sequence of completely standard computations. Indeed, (9)–(13) in step 1 is a Stokes problem while steps 2 and 3 are explicit computations. The convergence of Algorithm 3.1 is ensured by theorems [17,18] for all $r > 0$.

3.2. Mixed finite element approximation

Let a and b the following bilinear forms defined by:

$$a(\mathbf{u},\gamma;\mathbf{v},\delta) = 2r\int_\Omega (\gamma - D(\mathbf{u})) : (\delta - D(\mathbf{v}))\,\mathrm{d}x + 2\eta\int_\Omega \gamma : \delta\,\mathrm{d}x,$$

$$b(\mathbf{v},\delta;\sigma,p) = \int_\Omega \sigma : (D(\mathbf{v}) - \delta)\,\mathrm{d}x - \int_\Omega p\,\mathrm{div}\,\mathbf{v}\,\mathrm{d}x,$$

and j be the following convex l.s.c. proper functional

$$j(\gamma) = \sigma_0\int_\Omega \|\gamma\|\,\mathrm{d}x.$$

Then $(\mathbf{u},\gamma;\sigma)$ is a saddle-point of $\mathscr{L}_r$ if and only if it satisfies the following variational problem:

(FV) : find $(\mathbf{u},\gamma;\sigma,p) \in X_U \times T \times T \times L^2(\Omega)$ such that

$$\begin{aligned} j(\delta) - j(\gamma) + a(\mathbf{u},\gamma;\mathbf{v}-\mathbf{u},\delta-\gamma) + b(\mathbf{v}-\mathbf{u},\delta-\gamma;\sigma,p) &\geqslant 0,\\ b(\mathbf{u},\gamma;\xi,q) &= 0, \end{aligned}$$

for all $(\mathbf{v},\delta;\xi,q) \in X_U \times T \times T \times L^2(\Omega)$. Let $H_h \subset (H^1(\Omega))^2$, $D_h \subset T$, $T_h \subset T$ and $Q_h \subset L^2(\Omega)$ be some finite dimensional spaces. We introduce also $X_h = X_U \cap H_h$.

The finite dimensional version of the variational inequalities is simply obtained by replacing convex sets by their finite dimensional counterparts:

$(FV)_h$: find$(\mathbf{u}_h,\gamma_h;\sigma_h,p_h) \in X_h \times D_h \times T_h \times Q_h$ such that

$$\begin{aligned} j(\delta) - j(\gamma_h) + a(\mathbf{u}_h,\gamma_h;\mathbf{v}-\mathbf{u}_h,\delta-\gamma_h) + b(\mathbf{v}-\mathbf{u}_h,\delta-\gamma_h;\sigma_h,p_h) &\geqslant 0,\\ b(\mathbf{u}_h,\gamma_h;\xi,q) &= 0, \end{aligned}$$

for all $(\mathbf{v},\delta;\xi,q) \in X_h \times D_h \times T_h \times Q_h$.

The choice $D_h = T_h$ leads to $\gamma_h = R_h(D(\mathbf{u}_h))$, where R_h denotes the L^2 projection from T on T_h defined by

$$R_h\delta \in T_h \quad \text{and} \quad \int_\Omega (R_h\delta) : \xi\,\mathrm{d}x = \int_\Omega \delta : \xi\,\mathrm{d}x \quad \forall\xi \in T_h.$$

For $\sigma_0 = 0$ the problem reduces to a linear one that fits the theory of mixed finite elements (see e.g. [19]). In that case $\sigma_h = 2\eta D(\mathbf{u}_h)$ and the problem reduces to the following linear elliptic one:

$(S)_h$: find$(\mathbf{u}_h,p_h) \in X_h \times Q_h$ such that

$$\begin{aligned} 2\eta\textstyle\int_\Omega R_h D(\mathbf{u}_h) : D(\mathbf{v})\,\mathrm{d}x + 2r\int_\Omega (I-R_h)D(\mathbf{u}_h) : (I-R_h)D(\mathbf{v})\,\mathrm{d}x&\\ -\textstyle\int_\Omega p_h\mathrm{div}\,\mathbf{v}\,\mathrm{d}x &= 0,\\ -\textstyle\int_\Omega q\mathrm{div}\,\mathbf{u}_h\,\mathrm{d}x &= 0, \end{aligned}$$

for all $(\mathbf{v},q) \in X_h \times Q_h$. Clearly, when $R_h \neq I$ i.e. when $T_h \neq D(H_h)$ the discrete solution $\mathbf{u}_h$ depends upon the numerical parameter $r > 0$ of the augmented Lagrangian method. This property is not desirable. A necessary and sufficient condition for the solution $\mathbf{u}_h$ of $(FV)_h$ to be independent of the parameter r is $T_h = D(H_h)$. Then, problem $(S)_h$ reduces to a classical Stokes problem. Many pairs of spaces (H_h, Q_h) suitable for this problem can be found in [19]. In this paper, we choose the well-known Taylor–Hood finite element method.

Let $\mathscr{T}_h$ be a finite element mesh of Ω composed of triangles and let Ω_h be the resulting approximation of the domain Ω. We introduce the space H_h of continuous piecewise polynomial quadratic functions $(P_2 - C^0)$

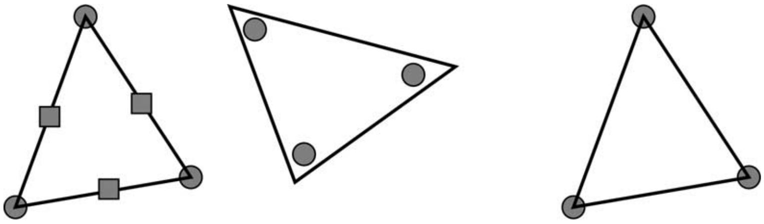

$\mathbf{u}$: $P_2 - C^0$ $\quad$ σ and γ: $P_1 - C^{-1}$ $\quad$ p: $P_1 - C^0$

Fig. 4. The finite element approximation.

and the space Q_h of continuous piecewise linear functions ($P_1 - C^0$). Thus $D_h = T_h = D(H_h)$ is the space of discontinuous piecewise linear function ($P_1 - C^{-1}$). Fig. 4 represents the mixed finite element approximation. It can be shown (see [20,21]) that the discrete problem $(FV)_h$ admits a solution with $\mathbf{u}_h$ and d_h uniquely determined. This quadratic approximation of the velocity field leads to high precision results and is well-suited to exhibit fine flow patterns.

3.3. Resolution of the Stokes subproblem

The finite element method leads to a discrete version of Algorithm 3.1. At step 1, we get a Stokes problem (9)–(13) discretized by the Taylor–Hood element. This gives the classical matrix problem:

$$\begin{pmatrix} A & B^{\mathrm{T}} \\ B & 0 \end{pmatrix}\begin{pmatrix} W \\ P \end{pmatrix} = \begin{pmatrix} F \\ G \end{pmatrix}$$

which is solved again by an Augmented Lagrangian algorithm [18].

Algorithm 3.2 (*Uzawa for Stokes*).

```
initialization $k = 0$
Let $P^0$ arbitrarily chosen.
loop $k \geqslant 1$
  • step 1: Let $P^k$ being known, find $W^k$ such that
      $(A + \tilde{r}B^{\mathrm{T}}B)W^{k+1} = F + B^{\mathrm{T}}G - B^{\mathrm{T}}P^k.$
  • step 2:
      $P^{k+1} := P^k + \tilde{r}BW^{k+1}.$
```

The parameter $\tilde{r}$ is fixed at 10^7, i.e. the inverse of the square root of the machine precision, in order to ensure very fast convergence of this subproblem. For the computation of W^{k+1}, the matrix $A + \tilde{r}B^{\mathrm{T}}B$ is factorized once and for all, before the global iteration of Algorithm 3.1, with a LDL^{T} method.

3.4. Using quadrature formulae for the constitutive equation

The explicit computation of γ^{n+1} at step 2 of Algorithm 3.1 is characterized as the solution of the following minimization problem:

$$\gamma^{n+1} := \underset{\delta\in T}{\arg\min}(\eta + r)\int_\Omega \|\delta\|^2\,\mathrm{d}x + \sigma_0\int_\Omega \|\delta\|\,\mathrm{d}x - \int_\Omega (\sigma^n + 2rD(\mathbf{u}^{n+1})) : \delta\,\mathrm{d}x$$

or equivalently, as the solution of the following variational inequality:

find $\gamma^{n+1} \in T$ satisfying for all $\delta \in T$

$$2(\eta + r)\int_\Omega \gamma^{n+1} : (\delta - \gamma^{n+1})\,\mathrm{d}x + \sigma_0\left(\int_\Omega \|\delta\|\,\mathrm{d}x - \int_\Omega \|\gamma^{n+1}\|\,\mathrm{d}x\right) \geqslant \int_\Omega (\sigma^n + 2rD(\mathbf{u}^{n+1})) : (\delta - \gamma^{n+1})\,\mathrm{d}x.$$

This variational inequality is approximated by replacing T by T_h and by using the following quadrature formulae on each triangle $K \in \mathscr{T}_h$:

$$\int_\Omega \gamma_K : \delta_K\,\mathrm{d}x \approx \frac{\mathrm{meas}(K)}{3}\sum_{i=1}^{3}\gamma_K(a_{i,K}) : \delta_K(a_{i,K}),$$

$$\int_\Omega \|\delta_K\|\,\mathrm{d}x \approx \frac{\mathrm{meas}(K)}{3}\sum_{i=1}^{3}\|\delta_K(a_{i,K})\|$$

for all γ_K, $\delta_K \in P_1(K)$, where $a_{i,K}$ denotes the ith vertex of the triangle K, $i = 1, 2, 3$. As a consequence, the discrete variational formulation leads to a discrete explicit expression similar to 3.1 on each vertex of each triangle of the mesh, since the approximation γ_h^{n+1} of γ^{n+1} is discontinuous and piecewise linear:

$$\gamma_{h|K}^{n+1}(a_{i,K}) := f(\sigma_{h|K}^{n}(a_{i,K}) + 2rD(\mathbf{u}_{h|K}^{n+1})(a_{i,K})) \quad \forall K \in \mathscr{T}_h,\ i = 1, 2, 3.$$

Thus the discrete version of the second step of Algorithm 3.1 is also explicit. Notice that the third step remains unchanged in the discrete version.

3.5. Mesh adaptation

A bidimensional anisotropic mesh generator BAMG [22] (see also Borouchaki et al. [23]) has been used. Let us first summarize on which principles this generator is based. Let $\mathscr{T}_0$ be an initial mesh and $\mathbf{u}_0$ be the solution of problem $(FV)_h$ associated to $\mathscr{T}_0$. Let φ_0 be the *governing field* to be suitably chosen from the solution $\mathbf{u}_0$.

The governing field φ_0 is approximated by a piecewise linear and continuous function $\varphi_{0,h}$ over each triangle $K \in \mathscr{T}_0$, and the error of interpolation in the unitary direction $\mathbf{d} \in \mathbb{R}^2$ is estimated by

$$e_{K,\mathbf{d}} = h_{K,\mathbf{d}}^2\left|\frac{\partial^2\varphi_0}{\partial\mathbf{d}^2}\right| \quad \text{in } K,$$

where $h_{K,\mathbf{d}}$ is the length of K in the $\mathbf{d}$ direction,

$$\frac{\partial^2\varphi_0}{\partial\mathbf{d}^2} = \mathbf{d}^{\mathrm{T}} \cdot H_{0,h} \cdot \mathbf{d}$$

and $H_{0,h}$ denotes a piecewise linear approximation of the Hessian of φ_0

$$H(\varphi_0) = \begin{pmatrix} \dfrac{\partial^2\varphi_0}{\partial x^2} & \dfrac{\partial^2\varphi_0}{\partial x\partial y} \\ \dfrac{\partial^2\varphi_0}{\partial x\partial y} & \dfrac{\partial^2\varphi_0}{\partial y^2} \end{pmatrix}.$$

The discrete Hessian $H_{0,h}$ is obtained from $\varphi_{0,h}$ by computing first the discrete gradient $\mathbf{g}_{0,h}$, continuous and piecewise linear, from the variational formula:

$$\int_\Omega \mathbf{g}_{0,h} \cdot \mathrm{v}_h\,\mathrm{d}x = \int_\Omega \nabla\varphi_{0,h} \cdot \mathrm{v}_h\,\mathrm{d}x,$$

where $\mathbf{v}_h$ is any continuous piecewise linear vector. Then $H_{0,h}$ is obtained from the variational formula:

$$\int_\Omega H_{0,h} : \tau_h \,\mathrm{d}x = \int_\Omega D(\mathbf{g}_{0,h}) : \tau_h \,\mathrm{d}x,$$

where τ_h is any continuous piecewise linear tensor.

Following Vallet [24], a possibility to adapt the mesh to the computation of φ_0 is to equi-distribute this error, i.e. to make it constant over all triangles and in all directions. Let λ_1, λ_2 be the eigenvalues of $H_{0,h}$ and $\mathbf{d}_1$ and $\mathbf{d}_2$ the associated eigenvectors:

$$\frac{\partial^2\varphi_0}{\partial\mathbf{d}_1^2} = \lambda_1 \quad \text{and} \quad \frac{\partial^2\varphi_0}{\partial\mathbf{d}_2^2} = \lambda_2.$$

The error $e_{K,\mathbf{d}}$ is independent of $\mathbf{d}$ and K when $e_{K,\mathbf{d}_1} = e_{K,\mathbf{d}_2}$, i.e. when

$$h_{K,\mathbf{d}_1}^2|\lambda_1| = h_{K,\mathbf{d}_2}^2|\lambda_2| = c_0 \quad \forall K \in \mathscr{T}_0,$$

where $c_0 > 0$ is a constant independent of K. The constant c_0 represents a global surface density factor: the adapted mesh generator tries to shrink elements in all directions with a factor $\sqrt{c_0}$ and element areas are thus reduced by a factor c_0.

The discrete Hessian $H_{0,h}$ being known over K, we suppose that $H_{0,h}$ is non-singular, i.e. $\lambda_1\lambda_2 \neq 0$. The constant c_0 being known, we want to build triangles of length h_i in the $\mathbf{d}_i$ direction with $h_i = \sqrt{c_0/|\lambda_i|}$, $i = 1,2$. Such a triangle has no privileged direction in a metric such that the two $h_i\mathbf{d}_i$ vectors, $i = 1,2$, have the same norm. Thus, we introduce the metric $M(\varphi_0)$, the eigenvectors as column of $H_{0,h}$ with the corresponding $|\lambda_1|$ and $|\lambda_2|$. The induced norm $\|\cdot\|_M$ satisfies

$$\|h_i\mathbf{d}_i\|_M = h_K\sqrt{\mathbf{d}_i^{\mathrm{T}} \cdot M(\varphi_0) \cdot \mathbf{d}_i} = \sqrt{c_0}, \quad k = 1,2.$$

Thus, an isotropic mesh in the Riemann space associated to the metric $M(\varphi_0)$ is a mesh extended in the Euclidean space with a factor h_i in the $\mathbf{d}_i$ direction.

It remains to choose a suitable φ_0. In the present case, this is a theoretical open problem. Several experiences of simulations have led us to the square root of the dissipative energy:

$$\varphi_0 = \left(\eta\|D(\mathbf{u}_0)\|^2 + \sigma_0\|D(\mathbf{u}_0)\|\right)^{1/2}.$$

The Hessian of such a governing field is expected to be singular in the vicinity of the boundary of the rigid zones, since the velocity solution of a Bingham flow problem is in general not in $H^3(\Omega)$. Hence, the generator will be forced to refine the mesh where accuracy is needed (see also [25]).

Solving a problem using a mesh adaptation is an iterative process, which involves three main steps:

1. Starting from an initial mesh $\mathscr{T}_0$, the problem is solved using the augmented Lagrangian algorithm. Let $\mathbf{u}_0$ be the corresponding solution associated to the mesh $\mathscr{T}_0$.
2. Let $\varphi_0 = \left(\eta\|D(\mathbf{u}_0)\|^2 + \sigma_0\|D(\mathbf{u}_0)\|\right)^{1/2}$ be the governing field. This field must emphasize regions where the solution has high gradients, so that the mesh generator refines these regions.
3. Starting from the governing field φ_0 on the mesh $\mathscr{T}_0$, the anisotropic mesh generator (see Borouchaki et al. [23] and Hecht [22]) generates a totally new mesh, denoted by $\mathscr{T}_1$.

Then, $\mathscr{T}_1$ is used to solve the problem, and so on, until the obtained solution gets clear limits between shear zones and rigid zones with no more jagged borders.

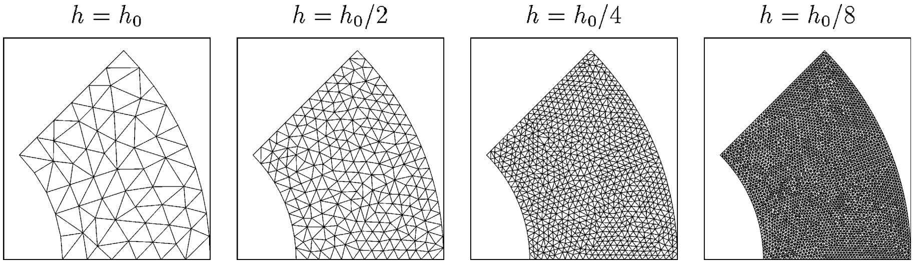

Fig. 5. Four quasi-uniform meshes used for the validation on the Couette flow.

3.6. Convergence tests with respect to mesh

Concerning the finite element approximation, sharp estimates are known in the case of a flow in a pipe (see Glowinski [26], Falk and Mercier [27], Glowinski et al. [15, Appendix 5] and Roquet et al. [25]). In more general cases (as the present case) Han and Reddy [28] have established a general error estimate on velocity and applied their estimate to the P_1-iso-P_1 approximation of the velocity–pressure. No estimate seems to be known about convergence with P_2 approximation of the velocity. Hence, it is necessary to check the convergence of the finite element approximation, in order:

(1) to validate our code,
(2) to estimate the order of convergence.

In the case of a Couette flow, the solution is explicitly known and it is possible to compute the following norms of the error $\mathbf{e}_h = \mathbf{u}_h - \Pi_h \mathbf{u}$

$$\|\mathbf{e}_h\|_{L^2} = \left(\int_{\Omega_h} \|\mathbf{u}_h - \Pi_h \mathbf{u}\|^2 \, \mathrm{d}x \right)^{1/2},$$

$$\|\mathbf{e}_h\|_{L^\infty} = \sup_{x \in \Omega_h} \|\mathbf{u}_h - \Pi_h \mathbf{u}\|,$$

$$\|\mathbf{e}_h\|_{H^1} = \left(\int_{\Omega_h} \|D(\mathbf{u}_h - \Pi_h \mathbf{u})\|^2 \, \mathrm{d}x \right)^{1/2},$$

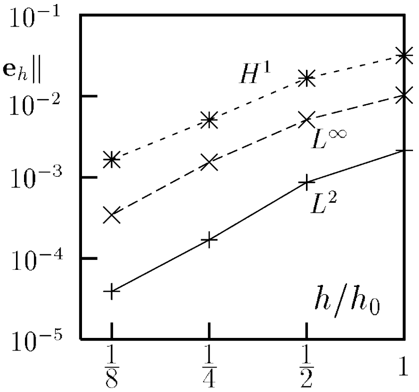

Fig. 6. Convergence curve: quasi-uniform meshes ($Bi = 10$).

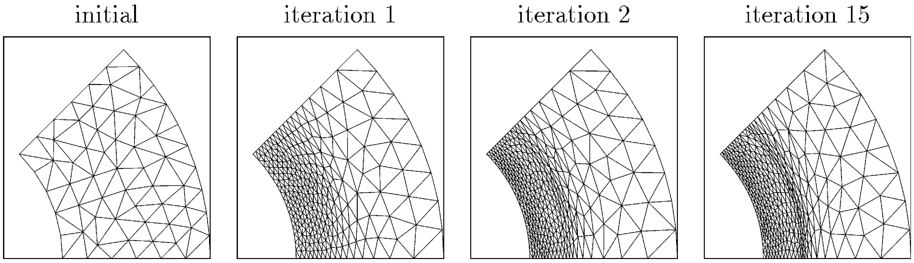

Fig. 7. Four meshes from the adaptation cycle used for the validation on the Couette flow.

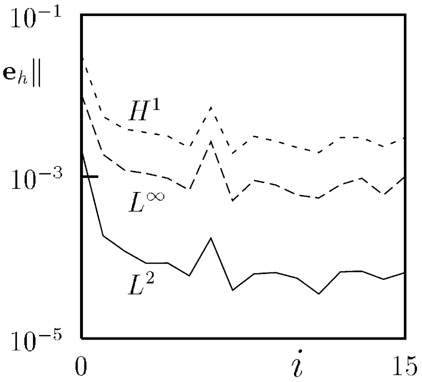

Fig. 8. Convergence curve: adaptive meshes ($Bi = 10$).

where $\Pi_h \mathbf{u}$ denotes the P_2 Lagrange interpolate of $\mathbf{u}$ on Ω_h. The error measure was first achieved on the quasi-uniform meshes presented in Fig. 5, and the convergence curve is shown in Fig. 6. We can clearly observe the convergence with an average rate of 1.43 for the energy norm. Furthermore, the efficiency of the adaptation process was measured; Fig. 7 shows some successive meshes of an adaptation cycle and Fig. 8 shows the error during this cycle. On these curves, the improvement of the accuracy is clear.

4. Numerical results

4.1. Determination of rigid zones

Rigid zones have been determined by using the Von Mises criterion, applied to the discrete field σ_h; the boundary of the rigid zones is then defined by the isovalue: $\|\sigma_h\| = \sigma_0$. The stream function is computed by a piecewise quadratic continuous approximation of the problem (see also Fig. 3):

$$-\Delta\psi = \operatorname{rot}\mathbf{u}_h \quad \text{in } \Omega,$$

$$\psi = -Ux \quad \text{on } \Gamma_{\mathrm{c}},$$

$$\psi = 0 \quad \text{on } \Gamma_\infty \cup \Gamma_w \cup \Gamma_y,$$

$$\frac{\partial\psi}{\partial\mathbf{n}} = 0 \quad \text{on } \Gamma_x.$$

This means in particular that we consider here the motion of the cylinder inside a material which is passive when away from the cylinder.

4.2. Effect of mesh adaptation

The different zones of the flow have very different sizes. In particular, the pike can be very small. Hence, it is important to have a well fitted mesh to know its shape accurately. This appears clearly in the works of Beris et al. where a well-suited mesh ([5], Fig. 3, p. 227) leads to the capture of the curvature of the pike (see Fig. 9, p. 233) and of the envelop, in the case of a spherical particle in an infinite medium. This idea is reinforced by the works of Blackery and Mitsoulis [7], where a non-adapted mesh leads to a less accurate solution (see the comparison of the two works in [7], Fig. 12, p. 74).

In the present work, an initial mesh is designed for each value of α. This mesh is purposely set uniform and coarse, in order not to influence the mesh adaptation process by presuming the aspect of the final solution. The purpose here is then to show that the mesh becomes automatically adapted to the sharper details (for instance, the shape of the pike), be the aspect of the solution known or not.

The initial meshes do not have the same size: the initial mesh size step $h^0 = h^0(\alpha)$ depends on α. Indeed, having h^0 constant (for different values of α) implies to take h^0 equal to the smallest value of α used (because at least an element is needed in the gap). This would lead to initial meshes with unnecessary high density if α is large. As for an example, if $h^0 = \alpha_{\min} = 1/16$, then 32 elements lie in the gap for $\alpha = 2$. This seems too dense for an initial mesh.

We have chosen $h^0(\alpha)$ such that:

$$h^0(\alpha) = \begin{cases} 1/2 & si \quad \alpha \geqslant 1/2, \\ \alpha & si \quad \alpha \leqslant 1/2. \end{cases}$$

Thus, there is at least one element in the gap for small values of α.

In what follows, except when otherwise is explicitly mentioned, the parameters are fixed to the values $\alpha = 1$ and $Bi = 10$. The value of the global mesh density parameter c_0, as introduced in paragraph 3.5, is fixed to $c_0 = 1/2$.

Fig. 9 shows how the solution improves in accuracy during an adaptation cycle. The initial mesh ($N = 0$) is coarse, hence, the envelop itself is very rough. Moreover, the almond and the pike do not appear on this first mesh. The second mesh ($N = 1$) is clearly more dense in the deformed zone, in particular in the gap. Hence, the almond appears on this mesh. In addition, the shape of the envelop becomes more distinct. The next mesh ($N = 2$) begins to be adapted to the different free boundaries. The shape of the envelop and of the almond are readable and the pike appears for the first time. The last mesh of the cycle ($N = 9$) is clearly strengthened on the free boundaries. It is also less dense than the second one ($N = 1$) in the parts of deformed zone where the energy dissipation is low (i.e. in the deformed zone but far from the gap).

The stream lines become readable faster than the boundaries of the rigid zones do, because the approximation of the stream function is more accurate (P_2) than the approximation of the stress tensor (P_1-discontinuous). In particular, the envelop and the boundary of the vortex can clearly be identified from the first adapted mesh.

Details of the mesh and of the boundaries of the rigid zones are exhibited in Fig. 10. It shows in particular that the triangles are stretched along the boundaries of the pike and the almond, and that these boundaries are smooth.

It means that the process used here allows one to determine very accurately the curvature of the free boundaries of the rigid zones. In particular, the specific case of Fig. 10 establishes clearly that the pike is not round and that the almond is convex, with pointed extremities.

Another important fact for the mesh adaptation process must be pointed out: the stress at the top of the cylinder (i.e. at the point facing the wall) is singular. It is then necessary to obtain a mesh fine enough and

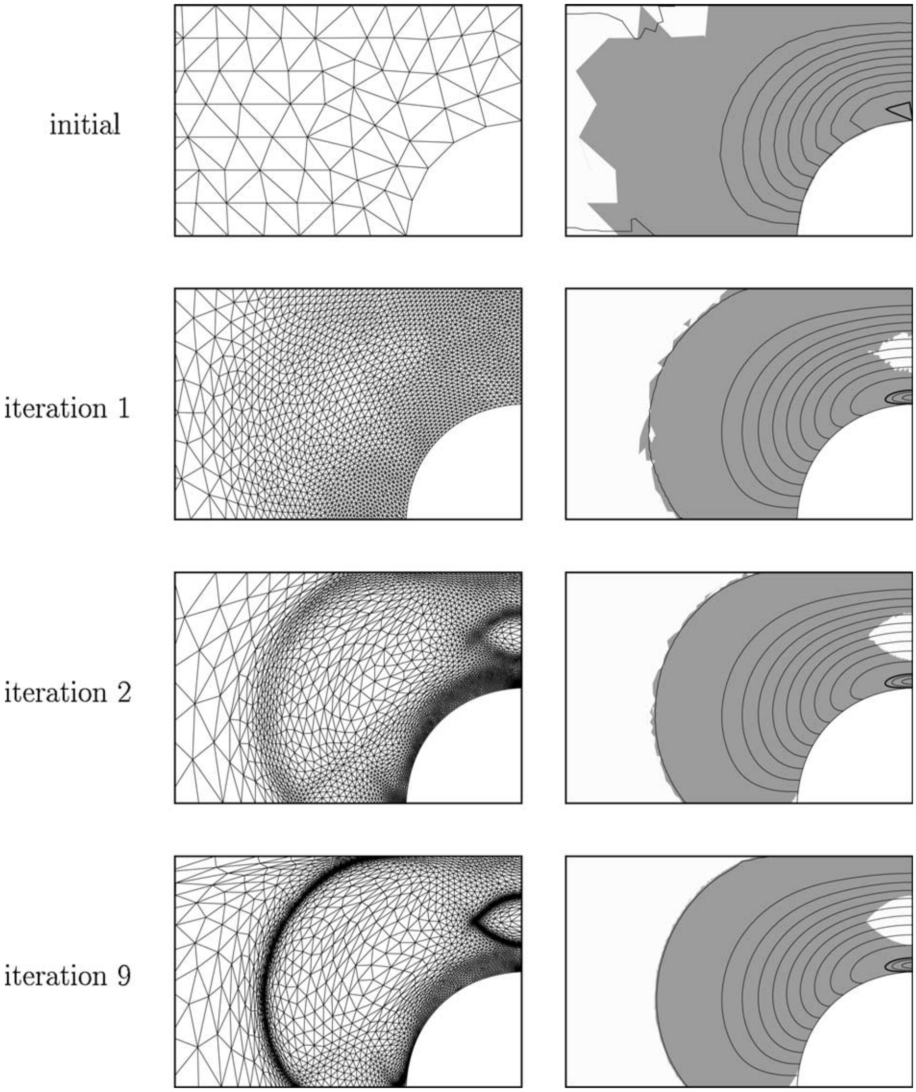

Fig. 9. Example of an adaptation cycle, $Bi = 10$ and $\alpha = 1$. Left column: four meshes of a neighborhood of the cylinder (cross section in white); Right column: corresponding to each mesh—rigid zones (light grey), deformed zone (dark grey), stream lines.

adapted to this singularity. Fig. 11a shows a zoom of the last mesh ($N = 9$) of the adaptation cycle, in the neighborhood of the singularity. In Fig. 11b, the quantity $\|\sigma\|$ is drawn on this area, along the symmetry axis (of the gap). The curve obtained shows the necessity of having triangles of size locally lower than 10^{-2} in order to catch the value of the singularity index. (Fig. 12).

In the particular case $Bi = 10$ and $\alpha = 1/4$, Fig. 13 shows how the profile of $\|\sigma\| - Bi$ improves in accuracy on the axis parallel to the direction of flow, when the global surface density factor varies: $c_0 = 2^{-n}$ for $n = 0, 1, 2$. The curve for $c_0 = 1$ is distinct from the two curves $c_0 = 1/2$ and $c_0 = 1/4$ which are almost the same. This points out an important fact: the convergence on this axis of the boundaries y_{p} of the pike and y_{e} of the envelop.

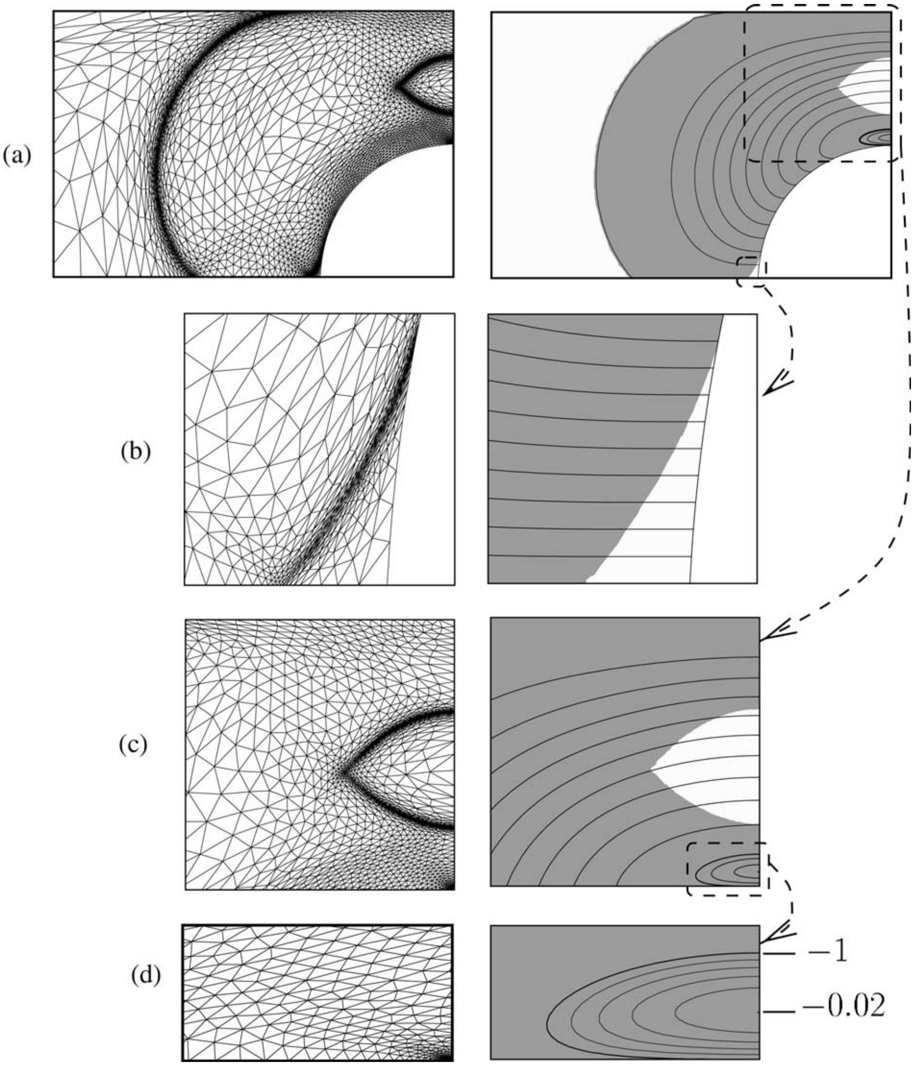

Fig. 10. Some specific aspects of the last mesh from a adaptation cycle ($Bi = 10$ and $\alpha = 1$); flow computed on this mesh (rigid zones in light grey, deformed zone in dark grey, streamlines): (a) global aspect; (b) zoom on the dead pike; (c) zoom on all the gap; (d) zoom on the vortex at the top of the cylinder.

4.3. When the cylinder becomes close to the wall

Let us now begin to observe the role of α in the different phenomena described above.

First, note in Figs. 14–16 that the decreasing of α leads to a reduction of the area of the almond, the pike and the deformed zone. In particular, the total width (in the direction of the flow) of the envelop is decreasing. Likewise, the almond flattens when α decreases and its oval (and pointed) shape is kept while its area reduces (Fig. 15). The pike also has a decreasing area while its shape is kept almost identical (Fig. 16). Notice that the almonds in Fig. 15 are shown magnified on the axis of the gap, i.e. the gap length α is represented with a constant length 1. This representation allows to compare the *relative size* of the almonds in the gap as α varies and to observe a clear reduction of this relative size when α decreases.

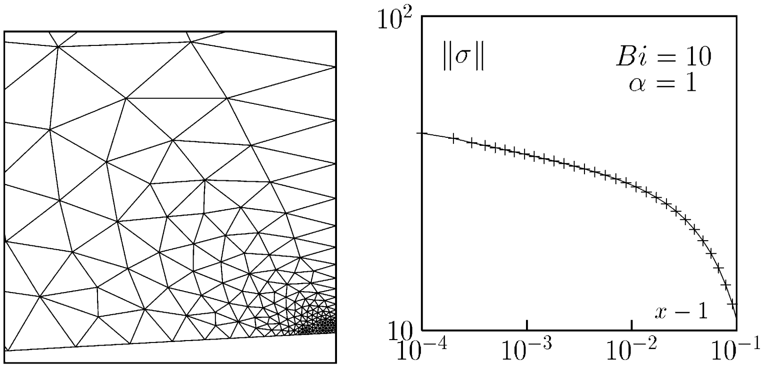

(a) (b)

Fig. 11. Neighborhood of the top of the cylinder ($Bi = 10$ and $\alpha = 1$): (a) zoom in the last mesh of an adaptation cycle; (b) singularity of $\|\sigma\|$.

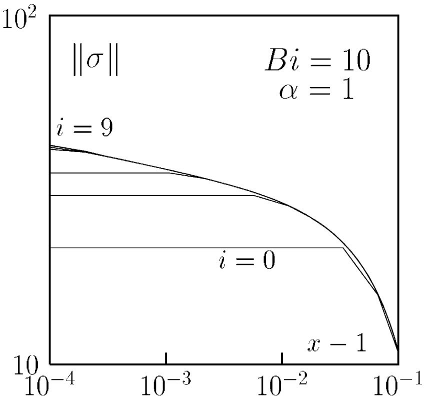

Fig. 12. Singularity of $\|\sigma\|$ near the top of the cylinder for the meshes ($0 \leqslant i \leqslant 9$) from an adaptation cycle ($Bi = 10$ and $\alpha = 1$).

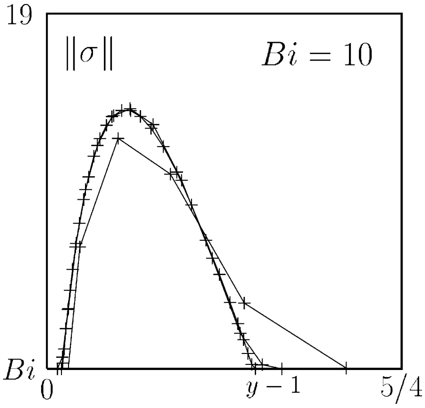

Fig. 13. Refinement of $\|\sigma\|$ on the flow axis, in front of the cylinder ($Bi = 10$, $\alpha = 1/4$ and $c_0 \in \{1/4; 1/2; 1\}$).

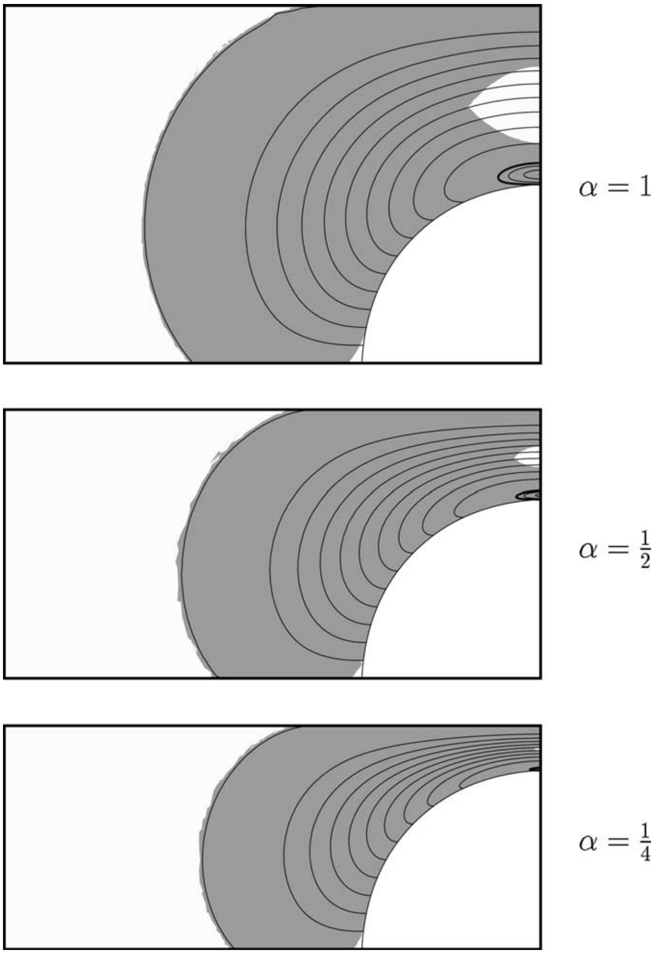

Fig. 14. Rigid zones (light grey), sheared zone (dark grey) and streamlines around the cylinder (white cross section), computed for some values of α and $Bi = 10$.

Let us consider the streamlines Fig. 14. These lines correspond to the trajectories of the particles of material whose motion is due to the one of the cylinder. Each particle thrown in front of the cylinder comes back to its initial position after the cylinder has passed. Two kinds of streamlines can be identified. On the one hand, some lines start horizontally from the cylinder, describe smooth curves which are surrounding the cylinder, and come back symmetrically in contact with it. In particular, the streamline $\psi = 10^{-6}$ underlines the boundary of the envelop. On the other hand, the velocity at the wall (of the plate) being zero, there exists another point on the axis of the gap where the velocity is again zero. The particles located between this particular point and the cylinder have a loop-like trajectory. Hence, this point where the velocity is zero is the center of a small vortex located just over the top of the cylinder. The boundary line of this vortex corresponds to the isovalue $\psi = -1$. In the gap, the streamlines grow closer as α decreases, showing the increasing of the shear-stress in this region. In Fig. 15, we can see that, for a fixed value of α, the distance between two consecutive streamlines remains constant, in accordance with the fact that the almond is a rigid zone. When α decreases, the vortex flattens while the value of ψ decreases in its center. This can mean an increasing shear-stress inasmuch as ψ does not decreases so fast (this aspect will be studied further with the velocity and the stress on the axis of the gap). In Fig. 16, the streamlines are

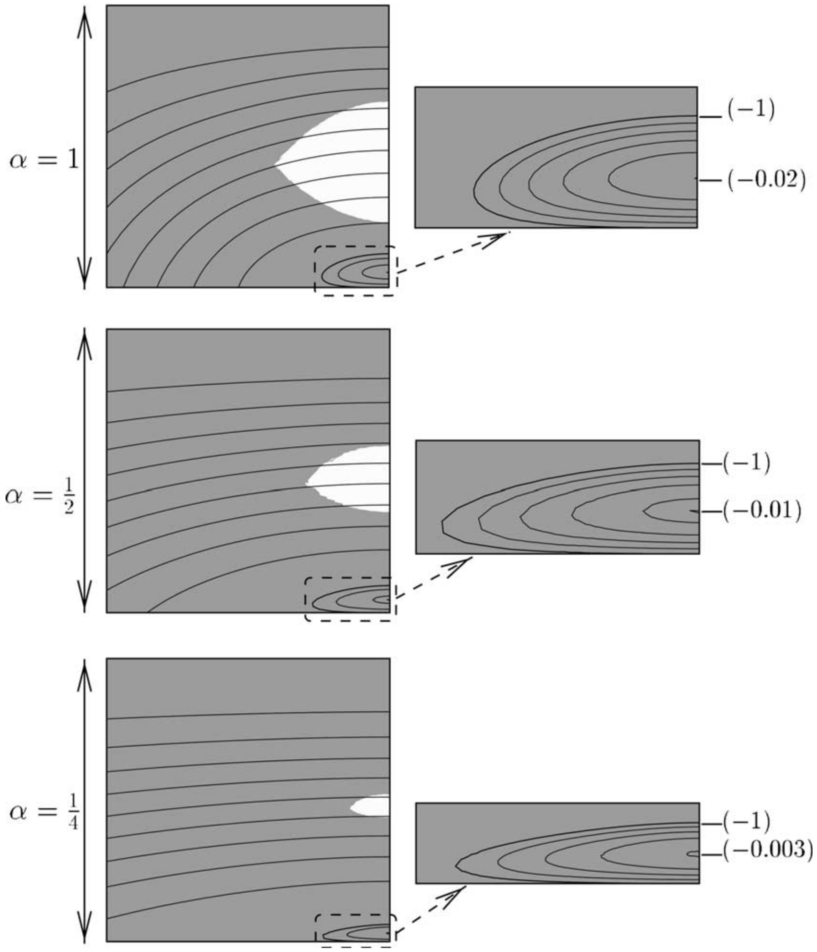

Fig. 15. Rigid almond (light grey), sheared zone (dark grey) and streamlines in all the gap, computed for some values of α and $Bi = 10$. Zoom on the vortex at the top of the cylinder.

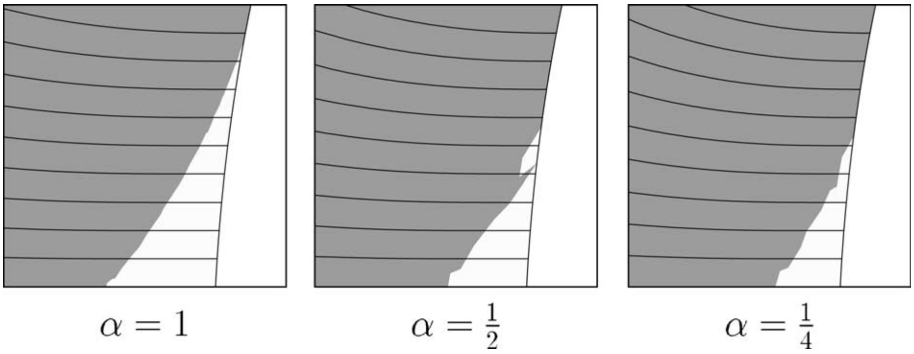
$\alpha = 1$ $\alpha = \frac{1}{2}$ $\alpha = \frac{1}{4}$

Fig. 16. Dead pike (light grey) sticked at the cylinder (white cross section), sheared zone (dark grey) and streamlines in front of the cylinder, computed for some values of α and $Bi = 10$.

horizontal in all the rigid region. Indeed, the velocity is constant and parallel to the axis of the flow in this zone because the pike is a dead zone with the same motion as the cylinder.

All those different aspects will be detailed and developed in the following sections.

4.4. Analysis of wall effect on velocity and stress

The purpose of this section is to study the geometric effects (i.e. the dependence on α), for $Bi \neq 0$. That is the reason why Bi has been fixed at a constant value: $Bi = 10$.

The geometric domain of computation was taken sufficiently long to ensure that the solution does not depend on it. In that purpose, the position y_e of the boundary of the envelop on the symmetry axis parallel to the flow was measured for different values of the length L (in the direction of this axis) of the domain. For each value of α, the computation has been achieved for $L = 10R$ and $L = 5R$: no significant changes were observed on the value of y_e. Hence the value $L = 5R$ was chosen.

4.4.1. Behavior along the axis of the gap

The behavior of the solution in the gap will now be considered in details. In particular, the variations of the stress and velocity along this axis will be observed. The *rescaled abscissa* $\tilde{x} = (x-1)/\alpha$ ($\in]0;1[$ for $x \in]1;1+\alpha[$) will be preferably used in order to make the comparison easier between those quantities for different values of α.

Let us first analyze how the stress tensor σ depends on α. Fig. 17a shows $\|\sigma\|$ along the symmetry axis (of the gap), for some values of α, with respect to the values of $\tilde{x} \in]0;1[$ (previously defined). Each curve grows to $+\infty$ when $\tilde{x}$ goes to 0, decreases to 0 at a point $\tilde{x}_1(\alpha)$, then $\|\sigma\| - Bi$ is positive again at a point $\tilde{x}_2(\alpha) > \tilde{x}_1(\alpha)$ and finally increases to a finite value at $\tilde{x} = 1$. This is due to three phenomena:

1. the stress is singular at the top of the cylinder (due to the geometry),
2. there exists a rigid zone (where $\|\sigma\| < Bi$), the almond, located in the middle of the gap,
3. the shear is high at the wall (due to the small value of α).

The shear raises at the wall when α decreases. This is characteristic in the wall affect, at least when no-slip condition is set at the wall (see for instance the works mentioned in introduction).

The singularity of the stress is also a well-known phenomenon for flows in this kind of geometry. Fig. 18a shows $\|\sigma\|$ in the neighborhood of the singularity, for some values of α. More precisely, near $x = 1$ we have:

$$\|\sigma(x)\| - Bi = c(\alpha)(x-1)^{-0.084},$$

$$c(\alpha) = c^* \alpha^{-4/5}, \quad \alpha \ll 1,$$

where c^* is a constant independent of Bi, α and x. The coefficient $c(\alpha)$ is shown in Fig. 18b.

The presence of the almond is less classical. The *relative size* of the almond defined by $\tilde{x}_2 - \tilde{x}_1$ decreases when α tends to 0, as shown in Fig. 17b. The evolution of the boundaries $\tilde{x}_1$ and $\tilde{x}_2$ is plotted with respect to the values α. When α decreases, the representative curve of $\tilde{x}_1$ raises and converges to the limit value $\tilde{x}_1(0) = 1/2$. On the other hand, the representative curve of $\tilde{x}_2$ can be split into two monotonic parts. For α decreasing to 1, $\tilde{x}_2$ is raised to a maximum. In a second part, when α tends to 0, $\tilde{x}_2$ decreases to the limit value $\tilde{x}_2(0) = 1/2$. Moreover, for $\alpha \leqslant 1$ the almond moves to the center of the gap, whereas for $\alpha \geqslant 1$ the almond is closer to the cylinder and further from the wall. In addition, for $\alpha \leqslant 1$, the relative size of the almond seems to tend to 0 when α tends to 0. This phenomenon is not obvious. Indeed, it would not have been irrelevant to consider the following hypothesis: the relative size $\tilde{x}_2 - \tilde{x}_1$ is a constant c. It would mean in fact that the "real" size of the almond is $x_2(\alpha) - x_1(\alpha) = c\alpha$ (and such a formula is possible if $c < 1$). In the present case, the almond flattens faster than the gap reduces. The evolution of the relative size of the

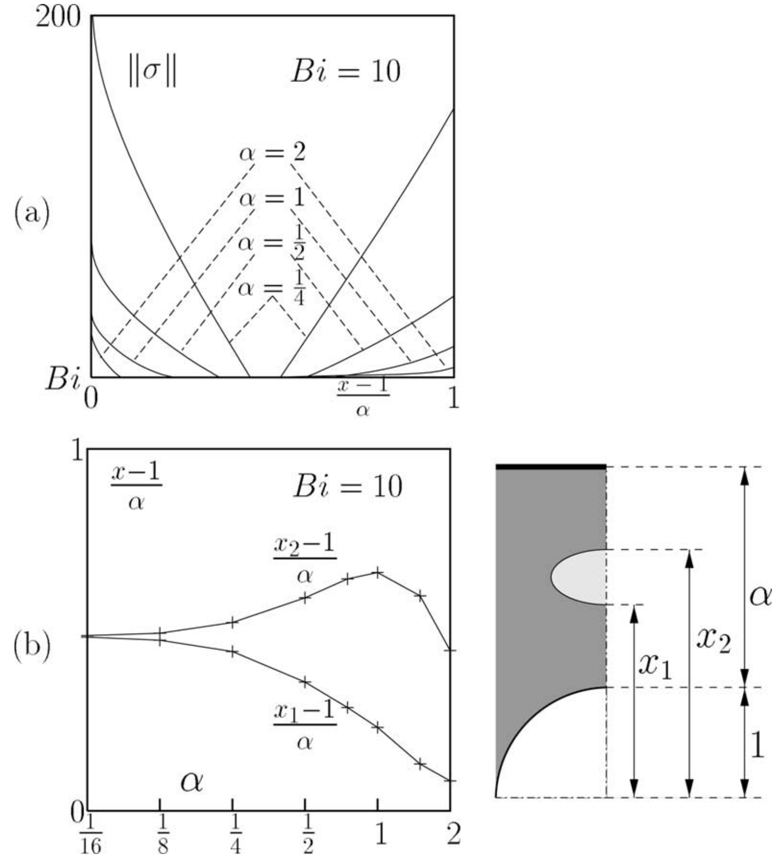

Fig. 17. Length of the rigid almond in the gap ($Bi = 10$): (a) $\|\sigma\|$ on the symmetry axis crossing the gap, for some values of α; (b) boundaries x_1 and x_2 of the almond on this axis as a function of α.

almond highlights the central role of the value $\alpha = 1$. This special value permits to separate situations "far from cylinder" ($\alpha \geqslant 1$) from situations "near the cylinder" ($\alpha < 1$).

Fig. 19 shows the velocity profile u_1 in the gap, along the symmetry axis, for some values of α. The curves look like a "tilted" mono-dimensional Poiseuille profile. More precisely, a slanted central plateau exhibits a solid rigid motion. This motion corresponds to the rigid almond (previously identified) and adds an information: the material is in rotation in this almond (the rotation rate being the slope of the plateau). Fig. 19b allows to compare the *relative length* of the plateau, with respect to the value of α. As already noticed with the analysis of the stress, the relative length decreases with α when $\alpha < 1$. This analysis of the velocity leads to study carefully the vorticity rot **u** (note that the comparison of the slope of the plateau is not obvious in Fig. 19b, because of the factor α in the rescaled representation with the abscissa $\tilde{x}$).

The field rot **u** is represented in Fig. 20 for some values of α. Again, a plateau occurs, corresponding to the slope of the plateau observed in the velocity profile. Hence, the value of rot **u** in the plateau is the rotation speed in the rigid almond.

The representation of rot **u** with respect to $\tilde{x}$, in the neighborhood of the plateau (Fig. 20c) shows the increase in the rotation speed ω in the almond, when α decreases. This increase is shown in Fig. 20d. The rotation speed ω tends to infinity when α tends to 0. More accurately, the following approximation holds:

$$\omega(\alpha) = c_1,\ \alpha^{-16/25}\alpha \ll 1.$$

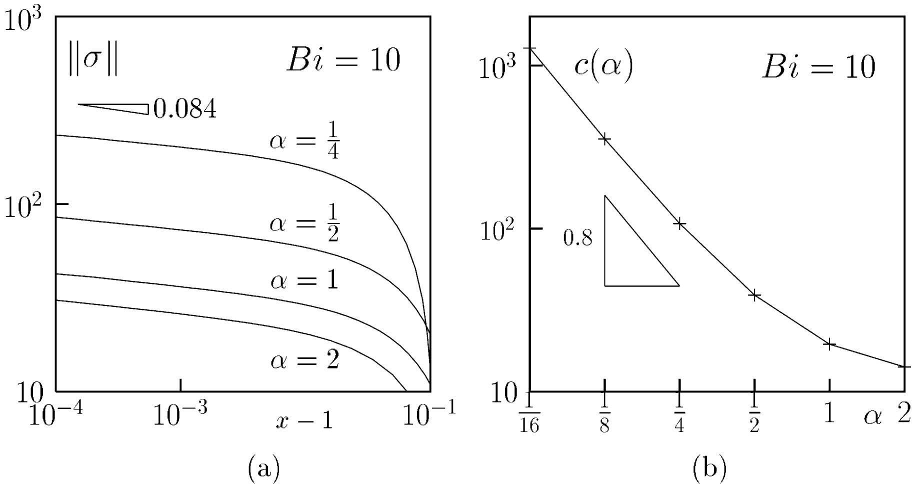

(a) (b)

Fig. 18. Singularity of $\|\sigma\|$ at the top of the cylinder ($Bi = 10$): (a) $\|\sigma\|$ on the symmetry axis crossing the gap, near the cylinder, for some values of α; (b) coefficient $c(\alpha)$ of the singularity in the formula $\|\sigma\| = c(\alpha)(x-1)^{0.084}$.

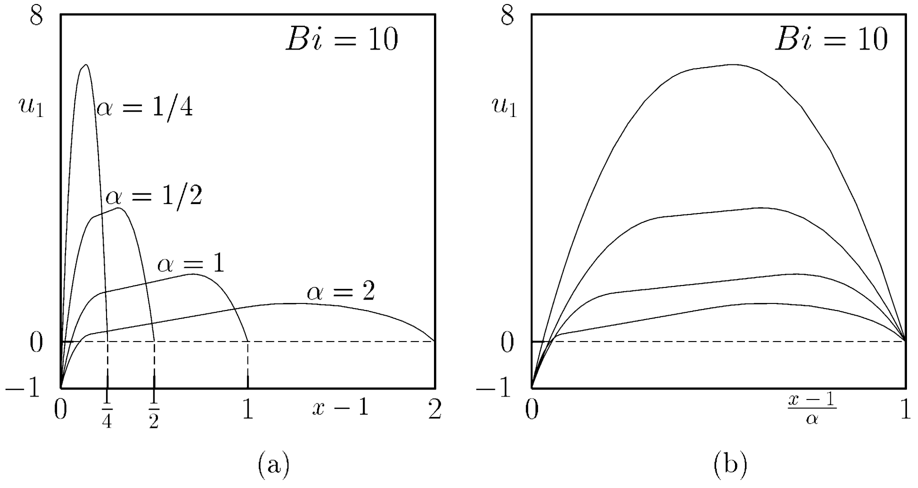

(a) (b)

Fig. 19. Velocity on the symmetry axis crossing the gap ($Bi = 10$) for some values of α: (a) superimposition of the curves; (b) rescaling of the gap from $]0;\alpha[$ to $]0;1[$.

4.4.2. *Behavior along the axis of the flow*

Let us now consider the behavior of the velocity and stress along the axis parallel to the direction of the flow.

Fig. 21a represents the velocity profiles on this axis, for several values of α. The velocity remains constant and equal to $-\mathbf{e}_2$ over a short distance near the cylinder, further the velocity increases until it reaches the constant value 0. The span over which the velocity changes is reducing when α tends to 0 and seems to reach a positive constant distance. This suggests that the deformed zone on this axis does not vanish.

Let us further observe the stress on this symmetry axis, for several values of α, Fig. 21b. Note the reduction of the length y_p of the pike and y_e of the deformed zone when α decreases. This is in good

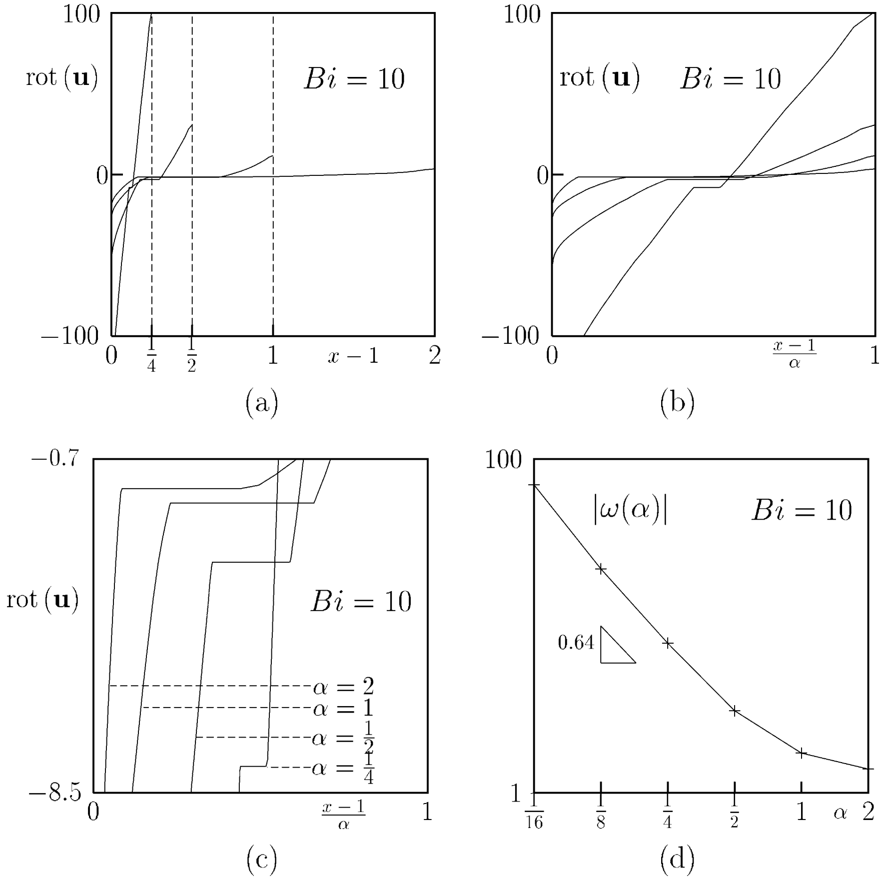

Fig. 20. Vorticity rot (**u**) on the symmetry axis crossing the gap ($Bi = 10$) for some values of α: (a) as a function of $x - 1$, (b) as a function of $\tilde{x}$, (c) zoom in the neighborhood of the plateau. (d) Rotation speed ω in the almond as a function of α.

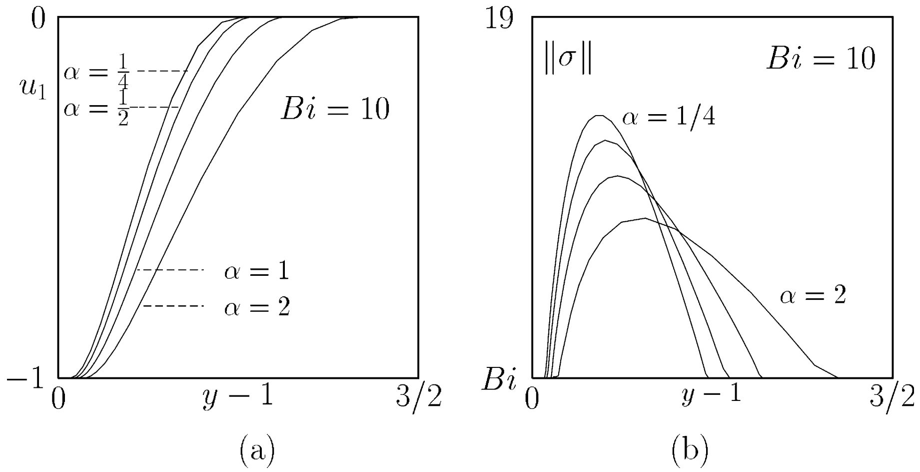

Fig. 21. Behavior around the cylinder, on the symmetry axis of the flow ($Bi = 10$), for several values of α: (a) velocity profile; (b) $\|\sigma\|$.

accordance with the previous observations on the velocity. In addition, when α reduces, the intensity of the stress increases. In particular, the maximum of $\|\sigma\|$ increases.

The length y_p of the pike and the length y_e of the deformed zone are shown, with their dependence on α, in Fig. 22. This confirms the previous observation that y_e and y_p tend to two distinct finite positive values when α tends to 0.

4.4.3. Drag coefficient

The drag coefficient has been computed following the definition (Batchelor [29], p. 229):

$$C_D = \frac{1}{\frac{1}{2}\rho U^2} \times \frac{1}{R} \times \int_{\Gamma^*_{cyl}} (\sigma^*_{\mathrm{tot}} \cdot \mathbf{n}) \cdot \mathbf{e_x} \, \mathrm{d}s^* = \frac{X}{\mathcal{R}e},$$

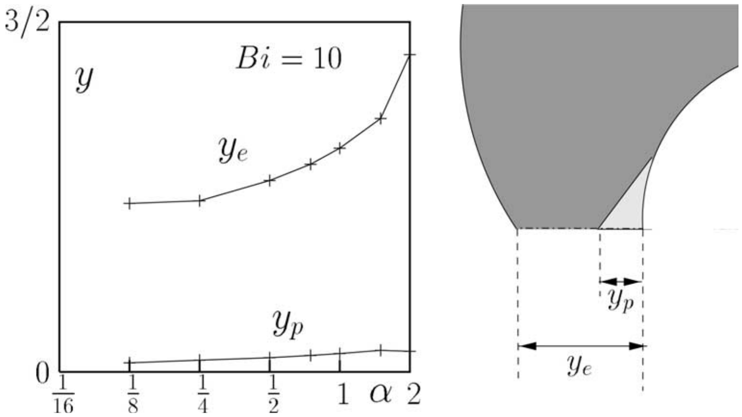

Fig. 22. Boundaries y_p of the pike and y_e of the envelop on the symmetry axis of the flow ($Bi = 10$), as a function of α.

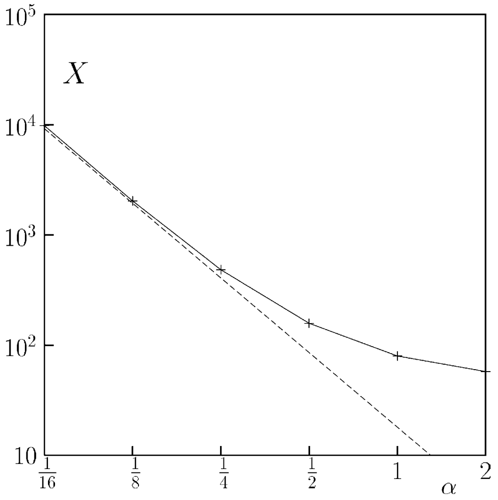

Fig. 23. Drag coefficient $C_X = X/Re$ as a function of α ($Bi = 10$).

where the star index * is related to dimensioned quantities and

$$X = \int_{\Gamma_{cyl}} (\sigma_{\mathrm{tot}} \cdot \mathbf{n}) \cdot \mathbf{e_x} \, \mathrm{d}s$$

is the quantity computed and shown in Fig. 23, with its dependence on α and for $Bi = 10$. This gives the asymptotic behavior of X, for $\alpha \ll 1$:

$$X = C\alpha^{-9/4}, \quad \alpha \ll 1.$$

5. Conclusion

The objective of this work is to compute the steady flow of a yield stress fluid around a cylinder. The development of macroscopic features, such as rigid zone enhancements is examined. An important result is the determination of the asymptotic behavior when the cylinder gets close the wall (i.e. α tends to zero). New results have been established at the vicinity of $\alpha = 0$ and are summarized as:

- The drag coefficient grows to infinity as $\alpha^{-9/4}$.
- The relative length of the almond tends to 0 and the vorticity inside it grows to infinity as $\alpha^{-16/25}$.
- The length of the pike and also the length of the envelop tend to finite and positive values, which are clearly distinct. The velocity profile also tends to a limit curve.
- The stress σ is singular at the top of the cylinder and the singularity index does not depend on α. The law describing $\|\sigma\|$ has been obtained in a neighborhood of the top of the cylinder, at the vicinity of $\alpha = 0$.

These new and sharp results confirm, in a complex case, the practical efficiency of the numerical resolution of the Bingham model, which was already analyzed in our previous works, from both theoretical [25] and numerical [30] points of view. The results of the present paper fully validate, to our opinion, the robustness and the accuracy of our numerical strategy. Our approach combines a high order mixed finite element approximation, an anisotropic auto-adaptive mesh procedure, and the augmented Lagrangian method. The adaptive strategy allows accurate capture of the yield surfaces, even in the difficult case when the cylinder becomes close to the wall.

References

[1] P.Y. Huang, J. Feng, Wall effects on the flow of viscoelastic fluids around a circular cylinder, J. Non-Newtonian Fluid Mech. 60 (1995) 179–198.
[2] N. Yoshioka, K. Adachi, On creeping flow of a viscoplastic fluid past a cylinder, Chem. Engrg. Sci. 28 (1973) 215–226.
[3] G.F. Brooks, R.L. Whitmore, The static drag on bodies in Bingham plastics, Rheol. Acta 7 (1968) 188–193.
[4] G.F. Brooks, R.L. Whitmore, Drag forces in Bingham plastics, Rheol. Acta 8 (1969) 472–480.
[5] A.N. Beris, J.A. Tsamopoulos, R.C. Armstrong, R.A. Brown, Creeping motion of a sphere through a Bingham plastic, J. Fluid Mech. 158 (1985) 219–244.
[6] M. Bercovier, M. Engelman, A finite element method for incompressible non-Newtonian flows, J. Comp. Phys. 36 (1980) 313–326.
[7] J. Blackery, E. Mitsoulis, Creeping motion of sphere in tubes filled with a Bingham plastic material, J. Non-Newtonian Fluid Mech. 70 (1997) 59–77.
[8] Papanastasiou, C. Tasos, Flows of materials with yield, J. Rheol. 31 (1987) 385–404.
[9] M. Beaulne, E. Mitsoulis, Creeping motion of sphere in tubes filled with Herschel–Bulkley fluids, J. Non-Newtonian Fluid Mech. 72 (1997) 55–71.
[10] R.P. Chhabra, P.H.T. Uhlherr, Static equilibrium and motion of spheres in viscoplastics liquids, Encyclopedia Fluid Mech. (1988) 611–633.
[11] D.D. Atapattu, R.P. Chhabra, P.H.T. Uhlherr, Wall effect for spheres falling at small Reynolds number in a viscoplastic medium, J. Non-Newtonian Fluid Mech. 38 (1990) 31–42.

[12] D.D. Atapattu, R.P. Chhabra, P.H.T. Uhlherr, Creeping motion in Herschel–Bulkley fluids: flow and drag, J. Non-Newtonian Fluid Mech. 59 (1995) 245–265.
[13] E.C. Bingham, Fluidity and Plasticity, McGraw-Hill, New York, 1922.
[14] J.G. Oldroyd, A rational formulation of the equations of plastic flow for a Bingham solid, Proc. Camb. Phil. Soc. 43 (1947) 100–105.
[15] R. Glowinski, J.L. Lions, R. Trémolières, Numerical Analysis of Variational Inequalities, North-Holland, 1981.
[16] M. Sofonea, I.R. Ionescu, Functional and Numerical Methods in Viscoplasticity, Oxford University Press, 1993.
[17] R. Glowinski, M. Fortin, Méthodes de Lagrangien Augmenté, applications à la résolution de problemes aux limites, Dunod, 1982.
[18] R. Glowinski, P. Le Tallec, Augmented Lagrangian and operator splitting method in non-linear mechanics, SIAM Studies Appl. Math. (1989).
[19] F. Brezzi, M. Fortin, Mixed and Hybrid Finite Element Methods, Springer-Verlag, 1991.
[20] N. Roquet, Simulation numérique d'écoulement de fluides viscoplastiques par un algorithme de lagrangien augmenté et une méthode d'éléments incompressibles, Rapport de DEA, Laboratoire d'analyse numérique d'Orsay, 1996.
[21] L. Boscardin, Méthodes de lagrangien augmenté pour la résolution des équations de Navier–Stokes dans le cas d'écoulements de fluide de Bingham, Thèse de doctoral, Université de Franche-Comté, 1999.
[22] F. Hecht, Bidimensional anisotropic mesh generator, INRIA, 1997.
[23] H. Borouchaki, P.L. George, F. Hecht, P. Laug, E. Saltel, Delaunay mesh generation governed by metric specifications. part I: Algorithms, Finite Elem. Anal. Des. 25 (1997) 61–83.
[24] M.G. Vallet, Generation de maillages anisotropes adaptés. Application à la capture de couches limites, Rapport de Recherche no. 1360, INRIA, 1990.
[25] N. Roquet, R. Michel, P. Saramito, Errors estimate for a viscoplastic fluid by using P_k finite elements and adaptive meshes, C.R. Acad. Set. Paris, Série I 331 (7) (2000) 563–568.
[26] R. Glowinski, Numerical Methods for Non-linear Variational Problems, Springer-Verlag, 1980.
[27] R.S. Falk, B. Mercier, Error estimates for elasto-plastic problems, RAIRO 11 (1977) 135–144.
[28] W. Han, B.D. Reddy, On the finite element method for mixed variational inequalities arising in elastoplasticity, SIAM J. Numer. Anal. 32 (1995) 1778–1807.
[29] G.K. Batchelor, An Introduction to Fluid Dynamics, Cambridge University Press, NY, 1981.
[30] P. Saramito, N. Roquet, An adaptive finite element method for viscoplastic fluid flows in pipes, Comput. Methods Appl. Mech. Engrg. 190 (2001) 5391–5412.